CO6-1 Effect of inter-protein interaction on SAXS profile in concentrated MurD solution

H. Nakagawa, T. Saio[1,2], M. Sugiyama[3], R. Inoue[3]

Materials Science Research Center, Japan Atomic Energy Agency
[1]Graduate School of Chemical Sciences and Engineering, Hokkaido University
[2]Department of Chemistry, Faculty of Science, Hokkaido University
[3]Institute for Integrated Radiation and Nuclear Science, Kyoto University

INTRODUCTION: In structural biology, precise determination of three-dimensional structures of proteins has been focused, and the structures with an atom-ic-resolution have given solid platforms to understand their biological functions. Recently, the idea of structural biology has extended beyond the static structural infor-mation with atomic resolution, in order to cover dynam-ical structures at different levels of space and time reso-lution. Neutron Spin Echo (NSE) is good methods to study the domain motions of a protein, where a relatively high concentrated protein solution, a few tens mg/ml, is often used [1]. In the high concentration, an effect of the inter-protein interaction on the NSE spectra as well as a small-angle scattering. In this study, the effect of the in-ter-protein interaction on Small angle X-ray scattering (SAXS) profiles were examined using MurD protein, which is a typical multi-domain protein (Fig.1) [2] and is good model to study the domain motion by NSE.

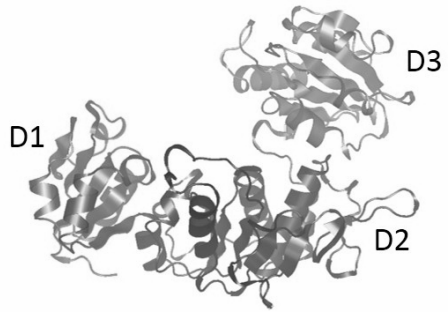

Fig. 1. Multi-domain protein, MurD, which are composed of three domains, D1, D2 and D3.

EXPERIMENTS: MurD were expressed in E. coli strain BL21 (DE3). SAXS were measured for MurD in apo state at the concentration of 5.0, 39.4 and 78.1 mg/ml. The buffer conditions were 20 mM Tris-HCl at pH=7.2.

RESULTS: SAXS profiles of MurD were successfully obtained for Apo state at various concentrations. Figure 2 shows the SAXS profiles. The inter-protein interaction effects were not observed in the SAXS profile at 5.0 mg/ml. At the lower Q region, at the higher protein concentrations, the intensity of SAXS decreased as a protein concentration increases. This should come from the inter-protein interaction. On the other hand, in the Q region above 0.08 Å^{-1}, all SAXS profiles almost coincided with each other. So, the higher concentration could not affect the conformation of a MurD protein molecule. These results suggest that the concentration effect on NSE spectra needs to be considered in the lower Q region than Q = 0.08 Å^{-1}. And at the higher Q region, NSE spectra can be analyzed without considering the concentration effect.

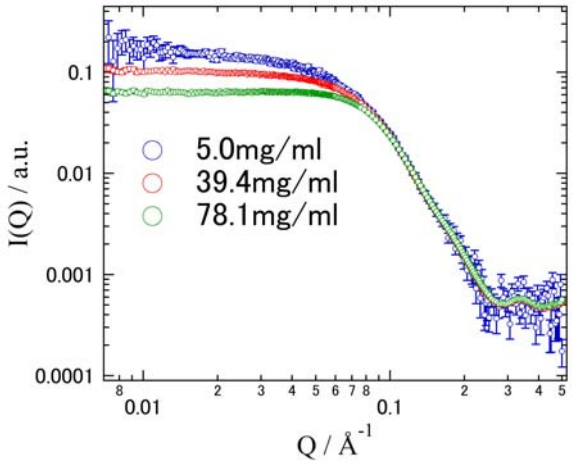

Fig. 2. SAXS profiles in MurD at several concentrations.

REFERENCES:

[1] R. Inoue *et al.*, Biophys. J. **99** (2010) 2309-2317.
[2] T. Saio *et al.*, Sci. Rep., **5** (2015) 16685.

CO6-2 Physicochemical study on ILEI suppressing amyloid-β generation

E. Hibino, K. Morishima[1], A. Okuda[1], R. Inoue[1], M. Sugiyama[1], and M. Nishimura

Molecular Neuroscience Research Center, Shiga University of Medical Science
[1]*Institute for Integrated Radiation and Nuclear Science, Kyoto University*

INTRODUCTION: The number of patients with Alzheimer's disease (AD) is increasing in Japan and AD is serious social issue. However, any effective AD-modifying drug is still undeveloped. The pathogenic processes of AD are considered to be triggered by accumulation of amyloid-ß protein (Aß) in brain. Previously, we have identified a secretory protein named interleukin-like epithelial-mesenchymal transition inducer (ILEI, also known as FAM3 superfamily member C (FAM3C)) as a negative regulator of Aß production by a novel activity[1]. ILEI is secreted from cell to bind to the extracellular region of Presenilin-1, a component of the γ-secretase complex. The interaction of ILEI with Presenilin-1 enhances nonspecific degradation of Aß precursor protein. ILEI was also reported ILEI C185A showed dysfunction of tumor growth, and metastasis[2]. However, the relationship of Aß production inhibitory activity and tumor growth and metastasis activity are still to be clarified.

The objective of this study is to elucidate struc- ture-function relationship that leads to develop a thera- peutic drug for AD. We especially analyzed basic struc- tural characteristics of wild-type and C185A mutant of ILEI and established experiment system.

EXPERIMENTS: Human wild-type ILEI and C185A mutant (residues 55-227) with hexahistidine tag were over-expressed in Rosetta-gamiB (DE3) pLysS stain and purified by Ni-NTA resin and size exclusion chromatography (SEC). CBB-stained SDS-PAGE gels on non-redox condition showed a single band.

For the MALDI-TOF/MS measurements, the purified proteins were directly transferred onto the 96 spotted polished steel target plate. After completely air drying, the plate was loaded to the Microflex LT (Bruker Daltonics, Bremen, Germany). The spectra were generated in linear positive ion mode.

For the structural characteristics, small-angle X-ray scattering (SAXS) measurements of the purified proteins at the concentrations of 1.0 mg/mL were performed with NANOPIX (Rigaku Corporation, Japan) at room temperature. The sample-to-detector distance and wavelength of X-ray used for present work was 650 mm and 1.542 Å, respectively. The scattering vector q covered from 0.02 to 0.3 $Å^{-1}$.

RESULTS: We previously measured 2D-NMR spectra of wild-type and C185A ^{15}N-ILEI. It was observed the positions of around 20 peaks were changing (data not shown). To confirm whether the differences are caused by overall conformational change or not, we firstly analyzed overall structural characteristics by MALDI-TOF/MS, analytical ultracentrifuge (AUC) and SAXS.

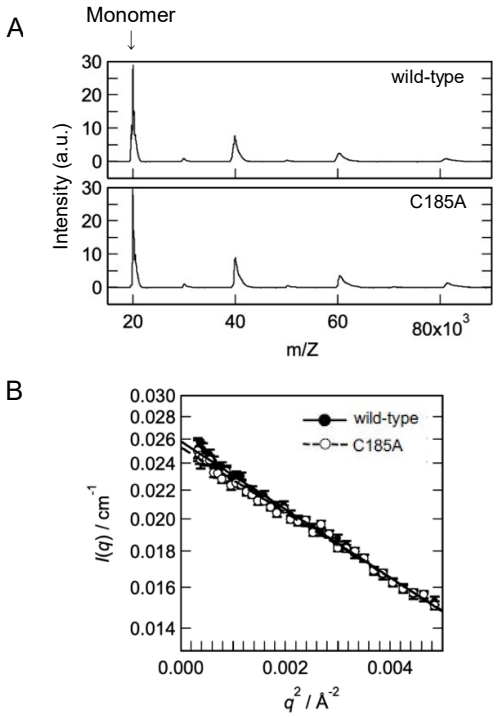

Fig. 1. (A) MALDI-TOF/MS measurements of wild-type and C185A mutant of ILEI indicated molecular weights of monomer and multimers.
(B) Gunier plots obtained from the scattering curves. in SAXS experiments.

The molecular weight of wild-type ILEI is around 20.0 kDa. The MALDI-TOF/MS measurements indicated that no difference of abundance ratio of monomer and multimer between wild-type and C185A mutant (Fig. 1A). The AUC experiments also supported the similar results (data not shown).

Furthermore, to confirm overall structural differences between wild-type and C185A mutant, SAXS experiments were conducted. From the Guinier analyzes of SAXS profiles of wild-type and C185A mutant of ILEI, no significant structural difference was observed between them (Fig. 1B). Namely, C185A mutation did not affect to overall structure of ILEI.

Through these integrative experimental approaches, it is expected that the NMR spectral change due to C185A mutation is caused by the local structural change.

We have already had dysfunctional mutants for Aß production inhibitory activity. We apply these analytical methods to these mutants for elucidation activity center of ILEI.

REFERENCES:

[1] H. Hasegawa *et al*., *Nat. Commun.*, 5:3917 (2014)
[2] M. Kral *et al*., *FEBS J*., **284** 3484–3505 (2017)

CO6-3 Structural characterization of circadian clock potein complexes

H. Yagi[1], Y. Yunoki[1,2], K. Morishima[3], A. Matsumoto[4], N. Sato[3], L. Porcar[5], A. Martel[5], R. Inoue[3], H. Kono[4], M. Sugiyama[3] and K. Kato[1,2]

[1]*Graduate School of Pharmaceutical Sciences, Nagoya City University*
[2]*Exploratory Research Center on Life and Living Systems, National Institutes of Natural Sciences*
[3]*Institute for Integrated Radiation and Nuclear Science, Kyoto University*
[4]*National Institutes for Quantum and Radiological Science and Technology*
[5]*Institut Laue-Langevin*

INTRODUCTION: The molecular machinery of the cyanobacterial circadian clock comprises three proteins: KaiA, KaiB, and KaiC. Through interactions among the three Kai proteins, the phosphorylation states of KaiC generate circadian oscillations *in vitro* in the presence of adenosine triphosphate (ATP). We especially focused on the KaiA-KaiB-KaiC ternary complex (ABC complex), which is considered to play the key role of the negative feedback loop of circadian rhythm. Recently, the cryo-electron microscopy (EM) structure of the ABC complex has been reported. However, the N-domains of KaiA subunits were poorly resolved due to their missing electron density maps. This observation probably reflected a high flexibility of linker between N- and C-domains. The whole structure of ABC complex has remained to be elucidated. Herein, for characterization of the overall structure of ABC complex, we conducted integrative techniques using small-angle X-ray scattering (SAXS), inverse contrast-matching small-angle neutron scattering (iCM-SANS), and native analytical ultracentrifugation (AUC) in conjunction with computer simulations.

EXPERIMENTS: The expression and purification of clock proteins, KaiA, KaiB and KaiC were performed according to methods previously described [1]. X-rays from a high-brilliance point-focused X-ray generator (MicroMAX-007HF, Rigaku, Tokyo, Japan) were focused with a confocal mirror (OptiSAXS) and collimated with a confocal multilayer mirror and two pinholes collimation system with the lower parasitic scattering, "ClearPinhole". The scattered X-rays were detected with a two-dimensional semiconductor detector (HyPix-6000, Rigaku, Tokyo, Japan). The sample-to-detector distance and wavelength of X-ray used for present work was 1320 mm and 1.542 Å, respectively. For removal of unfavorable aggregates from the sample solution, the laboratory-based SEC-SAXS System (LA-SSS) was employed to measure the SAXS profile in the Q range (0.01 $Å^{-1}$–0.2$Å^{-1}$). The SANS experiments were performed using the D22 instrument installed at the Institut Laue-Langevin (ILL), Grenoble, France. The sample-to-detector distance and wavelength of neutron used for present work was 5600 mm and 6.0 Å, respectively. SEC-SANS system was also utilized for present work.

RESULTS: The AUC data confirmed that KaiA, KaiB, and KaiC formed a 12:6:6 complex under the excess amount of KaiA.
With the aid of La-SSS, we succeeded to obtain mono-disperse ABC complex SAXS data. To obtain the structural information of subunits in the ABC complex in more detail, we also utilized the SEC-iCM-SANS. In this study, we prepared the ABC complex consisting of the 75% deuterated KaiB and KaiC subunits and the non-deuterated KaiA subunits. The solvent D_2O ratio at the contrast matching point was determined to eliminate scattering originating from the 75% deuterated KaiC subunits. As a result, we could exclusively observe the SANS profile from KaiA subunits in the complex.
Under the assumption of six-fold symmetry of arrangement of the 12 KaiA N-domain connected with EM structure of ABC complex, we made 20 million distinct structural models of the ABC complex. The SAXS and SANS scattering profiles were calculated for each model and compared with the experimental data. As shown in Fig. 1, the whole structure of ABC complex as well as the structural arrangement of the KaiA-N-domains in the complex was resolved.
In summary, we succeeded to solve the ABC complex structure using SEC-SAXS and SEC-SANS in conjunction with computer simulation. Present result should provide the insights into the working mechanisms of the circadian clock comprised of Kai proteins.

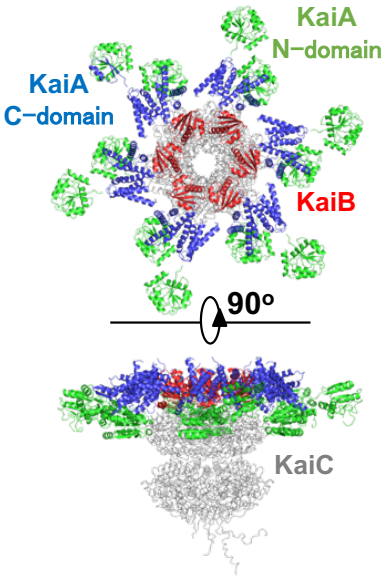

Fig. 1.
Structural model of KaiA-KaiB-KaiC complex based on the scattering data. N- and C-domains of KaiA, KaiB and KaiC are shown in green, blue, red and gray, respectively.

REFERENCES:
[1] M. Sugiyama *et al.*, Si. Rep., **6:35567** | (2016).

CO6-4 Interaction between Mint3 and FIH-1 involved in hypoxia stress responses

R. Maeda, S. Nagatoishi[1], K. Tsumoto[1], K. Morishima[2], R. Inoue[2], M. Sugiyama[2] and M. Hoshino

Graduate School of Pharmaceutical Sciences, Kyoto University
[1]Institute of Medical Science, the University of Tokyo
[2]Institute for Integrated Radiation and Nuclear Science, Kyoto University

INTRODUCTION: Oxygen is essential for many organisms to produce ATP efficiently from nutrients in food. Under the normal oxidative conditions, nutrients are metabolized through glycolytic pathway, tricarboxyl-ic acid cycle and electron transport system. Temporal or local drop of oxygen level induces cells to change the metabolic pathway, which is known as hypoxia stress responses. The responses are mainly triggered by hypoxia inducible factors (HIFs) that activate transcription of a group of genes.

Under the normal oxygen conditions, transcriptional activities of HIFs in the cells are inhibited by the factor inhibiting HIF-1 (FIH-1). On the other hand, several cells including tumor cells and macrophages, metabolize nutrients exclusively by nonoxidative glycolytic pathway even under the normal oxygen levels. Munc-18 interacting protein 3 (Mint3) is recently found to activate the hypoxia responses by binding and inhibiting the activity of FIH-1 in these cells [1]. Although the N-terminal 214 residues are found to be necessary for the interaction with FIH-1 to inhibit its activity, little is known about inhibitory mechanisms.

We attempted to elucidate the molecular mechanism of the interaction between Mint3 and FIH-1 by a various physicochemical methods, including small-angle X-ray scattering, analytical ultracentrifugation, and solution-state NMR.

EXPERIMENTS: High-expression systems for the N-terminal fragment proteins of Mint3 (Mint3(1–214) and Mint3(1–117)) and full-length FIH-1 were constructed by E. coli BL21 strains. The proteins were expressed in bacteria grown in LB-broth and ^{15}N-enriched M9 minimal medium to produce unlabeled and ^{15}N-labeled proteins, respectively.

NMR experiments were performed on a Bruker Avance 600 spectrometer equipped with a triple-resonance probe. A typical ^{1}H-^{15}N HSQC experiments were performed at protein concentration of 50 μM. The solvent conditions used were 20 mM sodium acetate (pH 7.3), and 10% D_2O. The chemical shift value was referenced to DSS.

RESULTS: We measured ^{1}H-^{15}N HSQC spectra of Mint3(1–214) and Mint3(1–117) proteins under the physiological conditions (pH 7.3). In both proteins, the chemical shift dispersion along the ^{1}H axis was small and most peaks were appeared within the range between 8.5 and 7.5 ppm, suggesting that the proteins were intrinsically disordered. This was also supported by the observation that the peak intensities were markedly decreased at higher temperature, probably rapid exchange of amide hydrogen with water molecules due to the lost of intramolecular hydrogen bonds.

Next, we measured the ^{1}H-^{15}N HSQC spectra of Mint3(1–214) and Mint3(1–117) in the presence of a various amount of unlabeled FIH-1. In both proteins, the intensities for several peaks were markedly decreased in a concentration-dependent manner, suggesting the involvement of specific binding of these residues. It should be mentioned that the same results were obtained both in Mint3(1–214) and Mint3(1–117), suggesting that the specific binding site for FIH-1 is present in a smaller fragment protein Mint3(1–117) (Fig. 1).

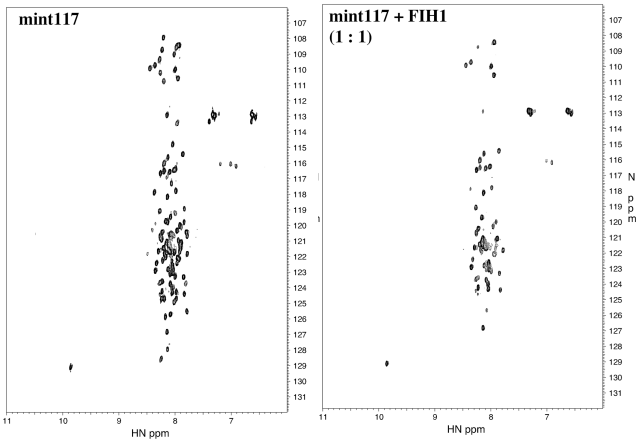

Fig. 1. ^{1}H-^{15}N HSQC spectra of Mint3(1–117) in the absence (left) and presence (right) of unlabeled FIH-1.

In order to elucidate the binding site at residue-level, we are now analyzing several 3D-triple resonance experiments, including 3D-HNCACB and 3D-hNcocaNH, to assign the resonance peaks. We are also attempting to analyze global change in the molecular shape of Mint3(1–214) / Mint3(1–117) and FIH-1 by small-angle X-ray scattering.

REFERENCES:

[1] Sakamoto *et al.,* (2014) Mol Cell Biol., **34 (1)** 30–42.

CO6-5 Supramolecular Tholos-Like Architecture Constituted by Archaeal Proteins Without Functional Annotation

M. Yagi-Utsumi, R. Inoue[1], M. Sugiyama[1] and K. Kato

Exploratory Research Center for Life and Living Systems (ExCELLS) and Institute for Molecular Science (IMS), National Institutes of Natural Sciences
[1]Institute for Integrated Radiation and Nuclear Science, Kyoto University

INTRODUCTION: Euryarchaeal genomes encode proteasome-assembling chaperone homologs, PbaA and PbaB, although archaeal proteasome formation is a chaperone-independent process. Homotetrameric PbaB functions as a proteasome activator, while PbaA forms a homopentamer that does not interact with the proteasome [1, 2]. Notably, PbaA forms a complex with PF0014, an archaeal protein without functional annotation. In this study, based on our previous research on PbaA crystal structure, we performed an integrative analysis of the supramolecular structure of the PbaA/PF0014 complex using native mass spectrometry, solution scattering, high-speed atomic force microscopy (HS-AFM), and cryo electron microscopy (cryo-EM).

EXPERIMENTS: For the purification of the PbaA/PF0014 complex, both recombinant proteins, PbaA (400 μM monomer) and PF0014 (400 μM monomer), were mixed at a 1:1 molar ratio and then dialyzed for 12 h against 50 mM Tris–HCl buffer (pH 8.0) containing 200 mM NaCl and 2 mM DTT.

SEC-SAXS measurements of the PbaA/PF0014 complex were obtained using UPLC ACQUITY (Waters) integrated with a SAXS set-up. In each measurement, 50 μL of 6 mg/ml proteins was loaded onto a Superdex 200 Increase 10/300 GL (GE Healthcare) pre-equilibrated with 50 mM Tris–HCl buffer (pH 8.0) containing 150 mM NaCl at a flow rate of 0.5 ml/min. During the elution of proteins, the flow rate was reduced to 0.10 ml/min. X-ray scattering and UV spectra were collected every 10 s.

For iCM-SANS experiments, a complex of 3 mg/ml of non-deuterated PbaA/75%-deuterated PF0014 as well as a complex of 75%-deuterated PbaA/75%-deuterated PF0014 was dissolved in 99.8% D_2O (ISOTEC) containing 50 mM Tris–HCl (pH 8.0) and 150 mM NaCl to reduce the incoherent scattering and obtain high-quality statistical data in the higher q-range. SANS experiments were performed using Quokka installed at the Australian Centre for Neutron Scattering (ANSTO, Sydney, Australia).

RESULTS: The results indicated that this highly thermostable complex constitutes ten PbaA and ten PF0014 molecules, which are assembled into a dumbbell-shaped structure. SEC-SAXS showed the PbaA-PF0014 complex exhibits an estimated radius of gyration (R_g) of 54.6 Å and maximum dimension (D_{max}) of 165 Å (Fig. 1). iCM-SANS, cryo-EM, and HS-AFM showed that two PbaA homopentameric rings correspond to the dumbbell plates, with their N-termini located outside of the plates and C-terminal segments left mobile. Furthermore, mutant PbaA lacking the mobile C-terminal segment retained the ability to form a complex with PF0014, allowing 3D modeling of the complex. The complex shows a five-column tholos-like architecture, in which each column comprises homodimeric PF0014, harboring a central cavity, which can potentially accommodate biomacromolecules including proteins. Our findings provide insight into the functional roles of Pba family proteins, offering a novel framework for designing functional protein cages [3].

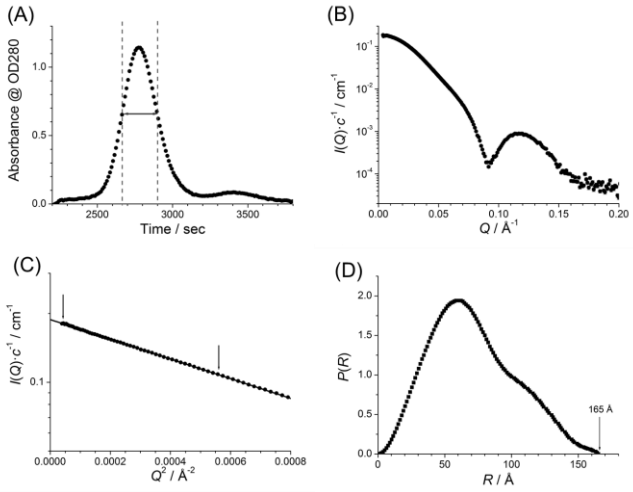

Fig. 1. (A) The SEC chart of the PbaA/PF0014 complex. We selected a region of full width at half maximum of the main peak from t = 2664 to t = 2900 s, indicated by red lines, for averaging the SAXS profile. (B) Averaged scattering profile. (C) Guinier plot indicating the range for the least square fitting by arrows and (D) distance distribution function, $P(r)$, of the averaged SAXS profile.

REFERENCES:

[1] A. Sikdar *et al.*, Biochem. Biophys. Res. Commun., **453** (2014) 493-497.
[2] M. Yagi-Utsumi *et al.*, Protein. Eng. Des. Sel., **31** (2018) 29-36.
[3] M. Yagi-Utsumi, *et al.*, Sci. Rep, **10**, (2020) 1540.

CO6-6

Small Angle X-ray Scattering Measurements on Insulin B-Chain Nucleation Intermediate Complexed with Fibrinogen

N. Yamamoto, E. Chatani[1], T. Akai[1], R. Inoue[2] and M. Sugiyama[2]

School of Medicine, Jichi Medical University

[1]*Graduate School of Science, Kobe University*

[2]*Institute for Integrated Radiation and Nuclear Science, Kyoto University*

INTRODUCTION: Amyloid fibrils are protein aggregates with β-sheet rich structure, which are associated with numerous amyloidoses and neurodegenerative diseases. Amyloid fibrils are typically formed through a nucleation-dependent mechanism. While a one-step nucleation is the simplest scheme, various oligomers have been identified in early stages, suggesting the presence of meta-stable nucleation intermediates [1].

In our previous work, we found that nucleation intermediates were formed in the early phases of amyloid fibril formation of an insulin-derived peptide, insulin B chain [2]. In addition, we found that fibrinogen, one of dominant plasma proteins, inhibits the formation of amyloid fibrils of insulin B chain by interacting with nucleation intermediates [3]. In this study, we elucidated structural properties of the nucleation intermediate by using small-angle X-ray scattering (SAXS) and analyzed change in SAXS profile after the addition of fibrinogen to elucidate the interaction manner of fibrinogen with the nucleation intermediate.

EXPERIMENTS: B chain was prepared from human insulin as described in a previous work [2]. The stock insulin B chain was diluted with 50 mM Tris-HCl buffer at a concentration of 1.4 mg/ml and was then put in a 1-mm path-length quartz cell. For the measurement of the B-chain nucleation intermediate, the sample was pre-incubated under quiescent conditions for 2 h at 25 °C. For the measurement of the complex with fibrinogen, a concentrated fibrinogen solution was added to the nucleation intermediate at the final concentration of 3.5 mg/ml approximately 5 min before the SAXS measurement. For the measurement of fibrinogen, a 3.5 mg/ml solution in 50 mM Tris-HCl buffer was used. SAXS profiles were measured at 25 °C with NANOPIX equipped with HyPix-6000 (Rigaku Corporation, Japan) with an exposure time of 30 min. A Cu K-α line (MicroMAX-007HF) was used as a beam source. The camera length was 1.33 m and the range of the scattering vector q was from 0.006 to 0.23 Å^{-1}.

RESULTS: Figure 1 shows the SAXS profile of the B-chain nucleation intermediate, fibrinogen, and the complex of the nucleation intermediate with fibrinogen. The slope of the log-log plot of the scattering profile of the nucleation intermediate was close to -1, suggesting a rod-like structure. As a result of the analysis of a cross-section plot for a cylindrical structure, it was suggested that the bottom radius is approximately 3 nm. It was also suggested that the length was approximately 270 nm based on Broersma's relationship [4] with a diffusion coefficient determined by DLS measurement. The rod-like structure was maintained even after the addition of fibrinogen, and the slope of the log-log plot kept close to -1. When the base radius and length of the complex were calculated in the same manner as for the nucleation intermediate, they were estimated to be 6 nm and 290 nm, respectively [5].

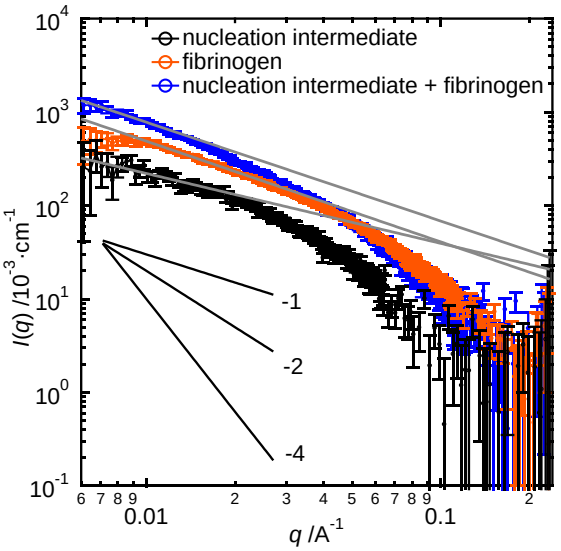

Fig. 1. One-dimensional SAXS profiles of the nucleation intermediate of insulin B chain (black), fibrinogen (orange) and the complex of the nucleation intermediate and fibrinogen (blue). Gray lines represent the slope of the profiles and the black slopes of -1, -2, or -4 indicate guides for the eyes.

The radius of fibrinogen was approximately 2.5 nm, and the increase in the radius by the fibrinogen binding could be explained reasonably when a single layer of fibrinogen molecules was assumed to surround the surface of the prefibrillar intermediates. It was thus suggested that fibrinogen binds to the surface of the nucleation intermediate so as to cover the surface of the nucleation intermediate, which would be the molecular basis of the inhibitory mechanism of B-chain amyloid fibril formation by fibrinogen. This structural insight of the B-chain nucleation intermediate complexed with fibrinogen will provide insights into general principles of functions of proteins that serve as chaperones or chaperone-like proteins involved in amyloid-related diseases.

REFERENCES:

[1] E. Chatani and N. Yamamoto, Biophys. Rev., **10** (2018) 527-534.
[2] N. Yamamoto *et al.*, Sci. Rep., **8** (2018) 62.
[3] T. Akai, Master's Thesis, Kobe Univ. (2017).
[4] S. J. Broersma, Chem. Phys., **32** (1960) 1632-1635.
[5] N. Yamamoto *et al.*, Biochemistry, **58** (2019) 2769-2781.

CO6-7 Character of DNA damage induced by nuclear palnt neutron beams

H. Terato, T. Saito[1], Y. Sakurai[1], T. Hanafusa, M. Isobe, S. Ihara[2] and Y. Tokuyama[3]

Advanced Science Research Center, Okayama University
[1]Institute for Integrated Radiation and Nuclear Science, Kyoto University
[2]Graduate School of Engineering, Saga University
[3]Analytical Research Center for Experimental Sciences, Saga University

INTRODUCTION: Radiation biological effects are arrived via DNA damaging by ionizing radiation, because DNA brings the genetic information. We have a lot of knowledge about radiation DNA damage. But the most of them were derived from gamma- and X-rays' studies with less information of other radiation qualities. Therefore, we have studied for the DNA damage with heavy ion beams, previously [1, 2]. These studies indicated that the DNA damage with heavy ion beams were unique, indicating that a lot of clustered DNA damage were generated including DNA double strand break (DSB), clustered base lesions, and these mixtures. Clustered DNA damage is a complex damage containing multiple lesions in the local region of DNA. This damage strongly inhibits DNA polymerization with high efficiently stopping of DNA polymerase moving on DNA. Also, clustered DNA damage shows less repairable, because there is no scaffold for DNA repair enzyme attaching. Here, we analyze the DNA damage with neutrons from nuclear power plant to unveil the molecular mechanism of neutron biological effect. The neutron beam is also high LET radiation as same as heavy ion beam. Therefore, we will find some interesting character of DNA damage with neutron like heavy ion beam. In the previous study period, we found the relatively higher yields of DNA damage with the neutron beams than gamma-rays. In this year, we estimated the cell viability for the neutron beams for the biological effect of this radiation.

EXPERIMENTS: Cultured cells of Chinese hamster ovary (CHO) AA8 strain were irradiated with neutron beams in the Kyoto University Reactor. The cells were cultivated with the conventional method. The logarithmic growing cells were recovered by trypsinization, and set into a polypropylene tube for irradiation. The irradiation time was up to three hours with sampling in every 30 minutes. The estimated dose rate of neutron was 1Gy h^{-1}. After irradiation, the cells were immediately dissolved again with the cultured medium and reseeded into fresh medium. The cells were cultivated for 10 days for growing the colony. The colony was fixed with ethanol and stained with methylene blue. The colony number was counted for estimation of the irradiated cell viability.

RESULTS: The result for cell viability indicated that neutron showed stronger cell damage ability than gamma-rays (Fig. 1). The surviving curve indicates that D_{37} of the neutron seems to be around 1 Gy. The dosimetry of the neutrons indicates that a half of dose of the reactor neutrons is derived from the contaminated gamma-rays (data not shown). Gamma-rays usually show that the D_{37} is around 4 Gy. This result suggests that the neutron has greater efficiency for the biological effect. We already have the result indicating that the neutron showed relatively higher efficiency to generate the DNA damage than gamma-rays. Thus, the severe biological effect with neutron beam seems to be derived from the higher yield of DNA damage.

In this yearly study, we obtained the relatively higher biological effect of the neutron. But, we need further study for elucidation of molecular mechanism of neutron biological effect. The first one is generalization of neutron effect. We are proceeding another neutron project at Kinki University Reactor (KUR). KUR generates weaker power neutron than the Kyoto University reactor. Comparing of the results with these two reactors will show a generalization of neutron efficiency. The second is analysis of DNA damage species with neutron beam. The future analyzing plan will contain the oxidative pyrimidine analysis such as 5-hydrooxycytosine. Also, the DSB will be analyzed by using of the mutant cell strains without homologous recombination (HR) and hon-homologous end joining (NHEJ). Using of these mutants leads the initial yields of DSB without DNA repair process.

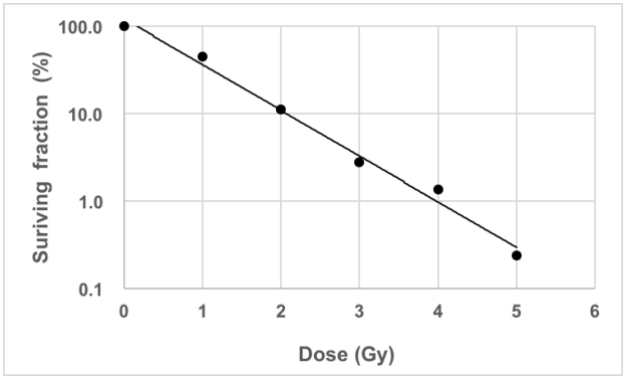

Fig. 1. Surviving fraction of the cells irradiated with the reactor neutrons.

REFERENCES:

[1] H. Terato *et al.*, J. Radiat. Res., **49** (2008) 133-146.
[2] Y. Tokuyama *et al.*, J. Radiat. Res., **56** (2015) 446-455.

CO6-8 Radiation-induced clustered DNA damage estimated by homo-FRET analysis

K. Akamatsu, N. Shikazono and T. Saito[1]

Institute of Quantum Life Science, National Institutes for Quantum and Radiological Science and Technology (QST)

[1]KURNS

INTRODUCTION:

DNA lesions induced by ionizing radiation and chemicals can cause mutation and carcinogenesis. In particular, "clustered damage" site, that is a DNA region with multiple lesions within one or two helical turns, is believed to hardly be repaired. This damage is considered to be induced, *e.g.*, around high-LET ionizing radiation tracks In fact, evidence is found in the direct observation AFM (atomic force microscopy) and a simulation [1]. However, detail of the damage is not known. We have already developed a method for estimating degree of localization of abasic sites (APs) in DNA using Förster resonance energy transfer occurred between different fluorescence probes ("hetero-FRET" using Alexa350 and Alexa488) [2]. The results showed that $^{12}C^{5+}$ beam produced close APs within a track: the apparent distance calculated was approximately 17 base pairs [3]. This finding indicates that direct radiation effect of $^{12}C^{5+}$ beam near the Bragg peak produces clustered DNA damage. We have recently applied the method to DNA in a cell-mimetic radical scavenging condition. However, there are some problems of the complex protocol and of the sensitivity due to the low extinction coefficient of Alexa350. We have, therefore, developed "homo-FRET" occurred between two or more Alexa488 molecules. We will obtain magnitude of FRET also from "fluorescence anisotropy" of homo-FRET between Alexa488 molecules. The new protocol using homo-FRET [4] enables us to estimate DNA damage localization without any enzymes and improves sensitivity to detect a clustered damage.

EXPERIMENTS:

●*Sample preparation and irradiation*

The plasmid DNA digested by Sma I was used (linear form). The DNA was dissolved to be ~10 mg/mL in 0.2 M Tris-HCl buffer (pH 7.5) which is a cell-mimetic condition in relation to radical scavenging capacity. Eight microliters of the DNA solution was transferred to a glass plate (10 mmϕ) under 100 % RH at r.t., and was irradiated with heavy ion beams, $^{20}Ne^{8+}$ (LET: ~500 keV/μm), $^{40}Ar^{13+}$ (LET: ~1800 keV/μm) at TIARA (QST), and ^{60}Co γ-rays (LET: ~0.3 keV/μm; KURNS) as a standard radiation source.

●*Preparation of fluorophore-labeled irradiated DNA and the FRET observation*

The damaged sample DNA (10 μL in water) and 10 μL of 100 mM Tris-HCl (pH 7.5) were mixed in a microtube. Two microliters of Alexa488/DMSO was added to the DNA solution and was incubated for 24 h at 35°C. The fluorophore-labeled DNA was purified by ethanol-precipitation followed by ultrafiltration. The fluorescence anisotropy was measured at 525 nm (ex. 470 nm).

The anisotropy, $< r >$, is defined as follows:

$$< r > = (I_{VV} - G\, I_{VH}) / (I_{VV} + 2G\, I_{VH}),$$

where I_{VV} is the fluorescence intensity when the excitation and emission polarizers are both vertically oriented. I_{VH} is one when the excitation/emission polarizers are vertically/horizontally oriented. G is the grating factor defined as I_{HV}/I_{HH}.

RESULTS AND DISCUSSION:

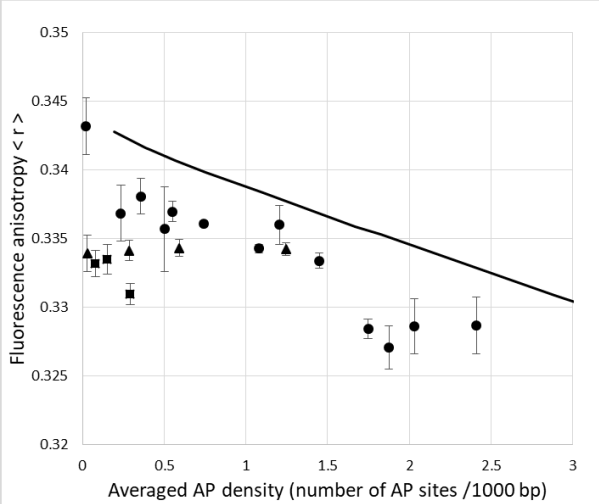

Fig. 1. Relationship between AP averaged density and fluorecence anisotropy for ^{60}Co γ-rays (●), Ne (▲), and Ar (■). The solid line indicates a theoretical curve when APs are randomly distributed.

In general, fluorescence anisotropy decreases with increasing FRET [5]. As shown in Fig.1, we found that the relationship differed significantly among the radiations tested. AP clustering even by the γ-rays seems to be more likely to occur than random distribution. Although the ion beams appeared to produce clustered AP more than the case of the γ-rays, the difference was not so significant that we expected from the results for the direct radiation effects using dry DNA samples [3]. Under cell-mimetic condition, most APs induced by the ion beams could exist as isolated lesions. Production of clustered APs by "indirect effect" (*e.g.*, by ·OH) may hardly occur due to recombination between radicals.

REFERENCES:

[1] Y. Matsuya, *et al.*, Int.J.Mol. Sci. 20, 1701.
[2] K. Akamatsu, N. Shikazono, Anal. Biochem., **433** (2013) 171-180.
[3] K. Akamatsu, N. Shikazono, and T. Saito, Radiat. Res., **183** (2015) 105-113.
[4] K. Akamatsu, N. Shikazono, Anal. Biochem., **536** (2017) 78-89.
[5] L. W. Runnels, and S. F. Scarlata, Biophys. J. **69** (1995) 1569.

Photoproduction of Medical ^{18}F and ^{99m}Tc Isotopes

M. Kurosawa[1], M. Fujiwara[1], N. Takahashi[1,2], M. Tamura[1], Y. Kosuge[2], N. Abe[3], T. Kubota[3], and T. Takahashi[3]

[1]*Research Center for Nuclear Physics, Osaka University*
[2]*Kyoto Medical Technology Co.*
[3]*Institute for Integrated Radiation and Nuclear Science, Kyoto University*

INTRODUCTION:

In the ^{18}F production, we use natural neon gas as a target in the gas recycling flow system. The ^{18}F-FDG pharmaceuticals are obtained by blowing small bubbles of irradiated neon gas in the glucose aqueous solution. In the ^{99m}Tc production, we use natural MoO_3. In both the methods, we can produce ^{99m}Tc isotopes for the SPECT inspections and ^{18}F isotopes for the PET inspections using the photoreaction on natural MoO_3 and Ne targets. We are going to polish up the usages of these two methods in view of practical aspect. .

^{18}F EXPERIMENT AND RESULTS

An electron beam from the linear accelerator facility at Institute for Integrated Radiation and Nuclear Science of Kyoto University (KURNS-LINAC) for producing RI from photoreactions. A 40 MeV electron beams with an intensity of 3-9 μA is used to bombard a platinum target with a thickness of 4 mm to generate bremsstrahlung photons for producing ^{18}F via the photoreaction on natural Ne gas.

The Ne gas circulation system has been developed for the present experiment. The irradiation time of bremsstrahlung photons was one hour. We expect that produced ^{18}F isotopes circulate with Ne gas, and that the monovalent -OH in glucose will be easily replaced by -^{18}F arrested in the liquid, resulting ^{18}FDG. The first purpose of the experiment was to examine this principle. Instead of glucose, we used a sodium hydroxide (NaOH) aqueous solution to trap ^{18}F. This seemed to be successful in ^{18}F collection.

However, when we used glucose instead of NaOH, the ^{18}F collection efficiency drastically decreased. The clear reason is still unknown. The reasons may come from 1) the intrinsic easiness of the chemical replacement reaction for the glucose and NaOH.

^{99m}Tc EXPERIMENT AND RESULTS

It had been reported that the high-rate production of ^{99m}Tc radioisotopes is realized by irradiating the bremsstrahlung photons on natural MoO_3 target [1,2]. We tried to develop the new method for extracting ^{99m}Tc using nano-particles.

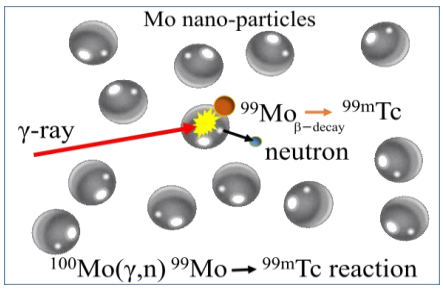

Figure 1: Photoreaction produces ^{99}Mo in nano-MoO_3 powder which has a porous assembly of many MoO_3. ^{99m}Tc radioisotopes decayed from ^{99}Mo are washed out using saline.

Figure 1 shows the schematics scheme for producing ^{99m}Tc via the $^{100}Mo(\gamma,n)^{99}Mo$ reaction. We notice that the size of the nano-particles is very small and the most of the ^{99}Mo produced by the photo-nuclear reaction can escape to the surface. Therefore, the produced ^{99m}Tc is easily separated from the $^{nat}MO_3$. If we pour the isotonic sodium chloride solution (saline) into nano-MoO_3 powder, ^{99m}Tc is readly soluble in saline even at the inside of nano-particles.

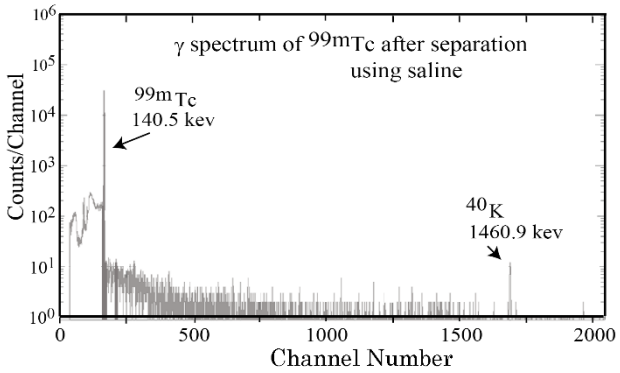

Figure 2: **γ**-ray spectrum measured with a Ge-detector after ^{99m}Tc separation using saline. Two prominent **γ**-ray peaks at 140.5 keV from ^{99m}Tc and at 1460.9 keV from ^{40}K as background are measured. The event yields lower than 140.5 keV are due to X-ray background from Pb shields and due to the Compton scattering of 140.5 keV γ-ray.

Figure 2 shows a γ-ray spectrum measured for the saline leaked out from the target vessel of MoO_3 nano-powder. Although we observe the backgrounds due to the X-rays from Pb-shields and due to the 1460.9 keV γ-ray from ^{40}K, it is clear that the saline leaked out from the target vessel includes only ^{99m}Tc (see the 140.5 keV peak).

REFERENCES:

[1] T. Takeda *et al.*, ^{99m}Tc production via the (γ,n) reaction on natural Mo, Journal of Radioanalytical and Nuclear Chemistry (2018) 318: 811-821.
[2] N. Takahashi, Patent Number 2014/05790.

CO6-10 Small Angle X-ray Scattering Measurements on Insulin B chain; a Time-Resolved Measure-ment to Monitor the Amyloid Fibril Formation via Prefibrillar Intermediates

N. Yamamoto, R. Inoue[1], K. Morishima[1], E. Chatani[2], and M. Sugiyama[1]

School of Medicine, Jichi Medical University
[1]*Institutute for Integrated Radiation and Nuclear Science, Kyoto University*
[2]*Graduate School of Science, Kobe University*

INTRODUCTION: Amyloid fibrils are abnormal protein aggregates associated with a numerous number of diseases called amyloidoses such as Alzheimer's disease. Amyloid fibrils generally possess fibrous morphology and β-sheet-rich structure, and the formation of amyloid fibrils typically follows a nucleation-dependent polymerization mechanism. It has been believed that the fibril formation occurs by one-step reaction from fibril nuclei. However, a variety of oligomers have been identified in early stages of fibrillation. Such oligomeric species attract attention as a key molecule in the nucleation process as well as molecular species responsible for cytotoxicity [1].

We recently found that prefibrillar intermediates were formed in the early phases of amyloid fibril formation of an insulin-derived peptide (insulin B chain) [2]. Especially, it was confirmed that two kinds of prefibrillar intermediates, i.e. the first prefibrillar intermediate and the subsequently-occurring second prefibrillar intermediate were formed. The structural detail of prefibrillar intermediates was elucidated using time-resolved small-angle X-ray scattering (SAXS) at the concentration of 1.4 mg/ml [3]. The analysis of the time-resolved measurement suggested elongation of the rod-like structure as the number of the second prefibrillar intermediate increased.

In this study, we also performed time-resolved SAXS experiment at the B chain concentration of 2.8 mg/ml to understand more detail about the elongation mechanism of the prefibrillar intermediates toward the fibril formation.

EXPERIMENTS: For the purification of B chain from human insulin, we followed the purification method of B chain described in literature [4]. The stock insulin B chain, which was dissolved in 10 mM NaOH, was diluted with 50 mM Tris-HCl buffer at a concentration of 2.8 mg/ml. The sample solution was then put in a 1-mm path-length quartz cell. SAXS profile was obtained at 25 °C with NANOPIX equipped with HyPix-6000 (Rigaku Corporation, Japan). A Cu K-α line (MicroMAX-007HF) was used as a beam source, which was further focused and collimated with a confocal multilayer mirror (OptiSAXS). The camera length was set to 1.33 m and the range of the scattering vector q was from 0.05 to 2.35 nm^{-1}. X-ray scattering data were collected with an exposure time of 30 min.

RESULTS: Fig. 1 shows time-resolved SAXS profiles of insulin B chain at the concentration of 2.8 mg/ml. It was demonstrated that the slope of the plot in the double-logarithmic scale was close to -1, indicating that the intermediates possess rod-like structures. A preliminary analysis of the cross-section plot, in which the intensity was plotted against q^2, was also performed to calculate the radius of the rod-like structure. As a result, it was demonstrated that the first prefibrillar intermediate was already formed even in the dead time of the measurement. It indicates that the increase in the concentration accelerated the formation of the first prefibrillar intermediate. Combined with a result of time-resolved dynamic light scattering measurement, it was also revealed that further elongation of the second prefibrillar intermediate occurred. This behavior supports our proposed idea that the formation of the amyloid fibril occurs via the second prefibrillar intermediate.

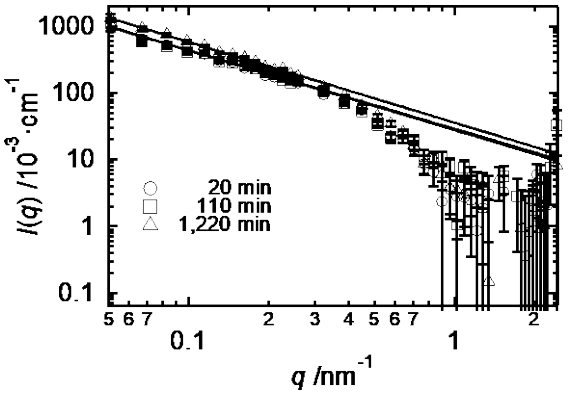

Fig. 1. Representative one-dimensional SAXS profiles of insulin B chain monitored at 20, 110, and 1,220 minutes. The lines indicate slopes obtained by curve fit.

REFERENCES:

[1] E. Chatani and N. Yamamoto, Biophys. Rev., **10** (2018) 527-534.
[2] N. Yamamoto *et al*., Sci. Rep., **8** (2018) 62.
[3] N. Yamamoto *et al*., KURNS PROGRESS REPORT 2018, CO6-7 (2018).
[4] N. Yamamoto *et al.,* Biochemistry, 58 (2019) 2769-2781.

CO6-11 Generation of radioresistant *Escherichia coli* by adaptive evolution using gamma rays as selection pressure II

T. Saito

Institute for Integrated Radiation and Nuclear Science, Kyoto University

INTRODUCTION: In nature, organisms have evolved diversely by adapting themselves to various environmental conditions. Some organisms have been found to survive in environments that can be easily perceived as extremely severe. Elucidating the adaptive mechanisms of organisms to severe environmental conditions can provide meaningful information regarding evolution and diversity overall. Some bacteria, known as radioresistant bacteria, demonstrate extreme resistance to ionizing radiations [1]. The extreme resistance mechanism of these bacteria to ionizing radiation is an interesting area of research from the standpoint of adaptive mechanisms employed by organisms in nature. In order to elucidate the mechanisms of radioresistance in these organisms, it is important to investigate their biological defense mechanisms against external stresses at the molecular level. However, studies conducted on radioresistant organisms existing in nature are likely to encounter many challenges due to limited knowledge of their genetic and biochemical properties. Therefore, in this study, the generation of radioresistant cells of *Escherichia coli* was attempted by experimenting on their ability to undergo adaptive evolution when exposed to gamma rays. The following operations were repeated in this experiment: gamma-ray irradiation of *E. coli* cells whose genetic and biochemical properties are sufficiently known, growth of the surviving cells, and irradiation of the grown cells. Furthermore, the gene expression status in evolved *E. coli* was analyzed and compared with that of wild type *E. coli*.

EXPERIMENTS: Evaluation of the sensitivity of *E. coli* cells to gamma irradiation: *E. coli K*-12 cells were grown to the early log phase in LB medium at 37°C at 200 rpm. One milliliter of the culture was centrifuged at 4000 × *g* at 20°C for 10 min. The supernatant was discarded and the pellet was suspended in 1 mL of PBS (–). The cell suspension was irradiated with gamma rays at a dose rate of 22 Gy/min at 20 ± 3°C. Gamma irradiation was carried out at the Co-60 Gamma-ray Irradiation Facility of the Institute for Integrated Radiation and Nuclear Science, Kyoto University. The gamma-irradiated cell suspension was diluted appropriately with PBS (–), plated on LB agar, and incubated at 37°C for 12 hr. After incubation, the colonies were counted, colony forming units were determined, and survival rates were calculated.

Selection with gamma rays: *E. coli K*-12 clone cells obtained by single colony pick-up were cultured to the early log phase in LB medium at 37°C at 200 rpm. The cell suspension was prepared as described above and irradiated with the 1% survival dose of gamma rays at a dose rate of 22 Gy/min at 20 ± 3°C. One milliliter of the gamma-irradiated cell suspension was inoculated in 100 mL of LB medium and cultured at 37°C at 200 rpm till the cells reached their early stationary phase. The glycerol stock was prepared and stored at –80°C. This procedure was repeated after culturing the glycerol stock cells to the early log phase.

Analysis of gene expression status: Total RNA was extracted from *E. coli* cells using RNAiso Plus (Takara), and further purified using NucleoSpin RNA Clean-up XS (Macherey-Nagel). The quality of the resulting total RNA was evaluated and confirmed with the Agilent 2200 TapeStation (Agilent). rRNA was removed from total RNA using Ribo-Zero Magnetic Kit (Gram-Negative Bacteria) (Illumina). The sequence library was prepared from the resulting RNA using TruSeq Stranded mRNA Sample Prep Kit (Illumina). The quality of the sequence library was evaluated and confirmed with the Agilent 2100 Bioanalyzer (Agilent). Sequence analysis was performed with NovaSeq 6000 (Illumina) and using NovaSeq 6000 S4 Reagent Kit (Illumina) and NovaSeq Xp 4-Lane Kit (Illumina). The gene expression levels were analyzed using Genedata Profiler Genome (Genedata) and STAR [2]. All procedures were done according to manufacturer's instructions.

RESULTS: The 1% survival dose to gamma rays of the wild type *E. coli* clone without selection was 240 Gy, whereas that of the *E. coli* population obtained after 20 selection cycles was 1900 Gy; the resistance of *E. coli* to gamma rays was increased 7.9-fold in this adaptive evolution experiment. The expression levels of 164 genes in the evolved *E. coli* were statistically significantly different from those in the wild-type *E. coli*. Among those genes, the expression level of 27 genes increased 2-fold or more, and the expression level of 23 genes decreased 0.5-fold or less. These results suggest that the radioresistance of the radioresistant *E. coli* obtained in this adaptive evolution experiment is attributed in part to these genetic changes. In the future, it is necessary to analyze in detail how these changes in gene expression are involved in the radioresistance of *E. coli*.

REFERENCES:

[1] T. Saito, Viva Origino, **30** (2007) 85–92.
[2] A. Dobin *et al.*, Bioinfomatics, **29** (2013) 15–21.

CO6-12 Structural study for the nucleosome containing histone variant H2A.B

R. Hirano[1], Y. Arimura[1], T. Kujirai[1], A. Okuda[2], K. Morishima[2], R. Inoue[2], M. Sugiyama[2], M. Koyama[1], and H. Kurumizaka[1]

Institute for Quantitative Biosciences, The University of Tokyo
[1]Department of Biological Sciences, The University of Tokyo
[2]Institute for Integrated Radiation and Nuclear Science (KURNS), Kyoto University

INTRODUCTION:
In eukaryotic cells, the genomic DNA is bound to histone proteins, and forms the chromatin structure [1]. The fundamental unit of the chromatin is the nucleosome, in which about 150-base-pairs of DNA are wrapped around the histone octamer containing two molecules of each four core histone (H2A, H2B, H3, and H4). The nucleosome generally prevents transcription factors from binding the genomic DNA. A group of the transcription factors, called pioneer transcription factors, are known to be able to bind their target DNA motifs in the nucleosome. The binding of pioneer transcription factors to the nucleosomes is reportedly influenced by histone variants, but the detail has not been understood. In this study, we focused on a histone H2A variant, H2A.B, as a representative for accessible nucleosome formation allowing transcription factor binding, and analyzed the solution structure of the nucleosome containing H2A.B by Small-Angle X-ray Scattering (SAXS).

EXPERIMENTS:
Canonical H2A, H2A.B, and $H2A^{H2A.B(103-115)}$ nucleosomes were prepared by the salt dialysis method with recombinant histones and DNA, as described previously [2]. The reconstituted nucleosomes were purified by non-denaturing gel electrophoresis. SAXS analyses of these nucleosomes were performed with a NANOPIX instrument (RIGAKU) at the Institute of Radiation and Nuclear Science, Kyoto University [3]. In order to cover the wide *q*-range, we analyzed these nucleosomes with two sample-to-detector distance (1,330 mm for 0.007 $Å^{-1}$ to 0.03 $Å^{-1}$, and 300 mm for 0.03 $Å^{-1}$ to 0.8 $Å^{-1}$) and then combined these data. We also performed the standard procedures of transmission correction, buffer solution of these nucleosomes scattering subtraction, and conversion to an absolute scale with water scattering.

RESULTS:
We measured the SAXS curves of H2A, H2A.B, and $H2A^{H2A.B(103-115)}$ nucleosomes, and calculated the values of the radius of gyration (*Rg*). We found that the *Rg* value of the H2A.B nucleosome was significantly larger than that of the canonical H2A nucleosome. This suggested that the H2A.B nucleosome is not compact as H2A nucleosome (Fig. 1). Interestingly, the *R*g value of the $H2A^{H2A.B(103-115)}$ nucleosome was also significantly larger than that of the canonical nucleosome. Therefore, the C-terminal region of H2A.B may play a role in forming apparently large conformation in solution (Fig. 2).

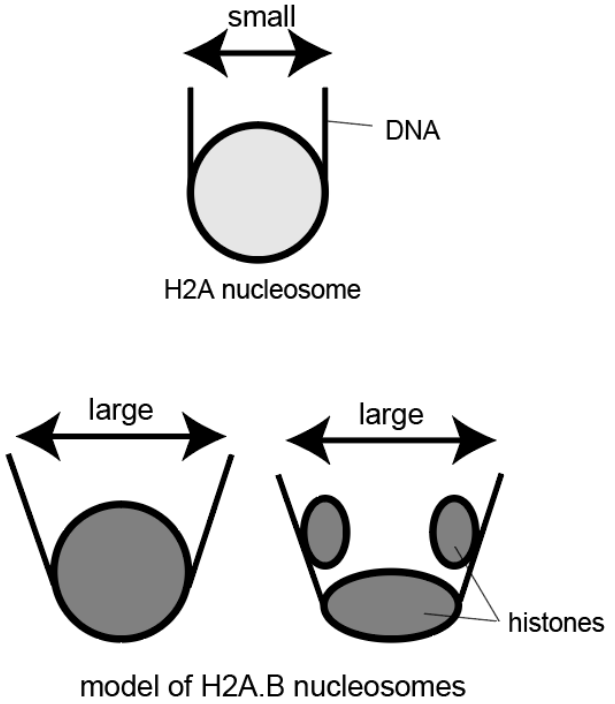

Fig.1 The schematic representations of the conceivable relationship between the *Rg* value and the nucleosome structure in SAXS analysis.

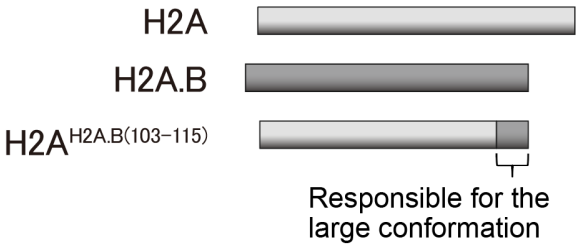

Fig.2 Schematic representations of H2A, H2A.B, and $H2A^{H2A.B(103-115)}$.

REFERENCES:
[1] M. Koyama and H. Kurumizaka, J. Biochem. **163** (2018) 85-95.
[2] T. Kujirai *et al*., Methods Mol. Biol. **1832** (2018) 3-20.
[3] P. Bernadó *et al*., Biochim. Biophys. Acta. Gen. Subj. **1862** (2018) 253-274.

CO6-13 Effect of High-Intensity Pulsed Coherent Radiation on the Stability of the Gene

Y. Tanaka, S. Okuda and T. Takahashi[1]

Graduate School of Engineering, Osaka Prefecture University

[1]*Institute for Integrated Radiation and Nuclear Science, Kyoto University*

INTRODUCTION: The coherent transition radiation (CTR) from electron bunches of a linear accelerator (linac) has continuous spectra from a submillimeter to millimeter wavelength range corresponding to the terahertz (THz) frequency range. It is a picosecond pulsed light and hence, has extremely high peak-intensities compared with the other THz light sources. The light source system using the CTR from the electron beams of the 45 MeV L-band electron linac was established at Kyoto University Research Reactor Institute (KURRI) [1-3]. This CTR light source developed has been applied to absorption spectroscopy. Recently, the possibility of any nonlinear effects was found in the measurement of the absorption spectroscopy at KURRI.

However, biological effects of the radiation are unclear. The main purpose of the present work is the investigation of the biological effects of the high-intensity pulsed CTR using a gene of fruit fly, *Drosophila melanogaster.*

EXPERIMENTAL METHOD: The electron linac at KURRI was used in the experiments. In most experiments the beam energy, macropulse length and the repetition rate are 42 MeV, 47 ns and 60 Hz, respectively. The experimental configurations for the absorption spectroscopy are schematically described in our previous report [4] and the details of the methods for the measurements are described in ref. 2 and 3.

The detection method of effect on the stability of the gene was performed using the *mwh* (*multiple wing hair*) gene of *Drosophila melanogaster* as described in ref. 5. If the CTR have any effect on the gene, the mutation frequency rate will increase or decrease. The frequency is calculated as the small spot or large spot rates. The irradiation experiment was performed by packing the larvae in a container with glass, plastic cylinder and sponge, then the larvae were put in the path of the CTR, while the non-irradiated control larvae were put near the irradiated sample outside the path. Duration of irradiation was 2, 4 and 6 hrs. After irradiation the larvae were transferred into new culture vials.

RESULTS AND DISCUSSION:

As shown in Fig.1, by irradiation of CTR for 2 and 4 hours, the small spot rate apparently increased compared with the non-irradiated control groups, while the large spot rate decreased compared with the non-irradiated control groups, however, this phenomenon seems to be within the variation because the large spot number was very scarce. By irradiation of CTR for 6 hours, both of small spot rate and large spot rate were similar with the non-irradiated control groups. Thus, irradiation of CTR for 2 and 4 hours could cause mutation or deletion of the wild-type *mwh* gene, or chromosomal disjunction.

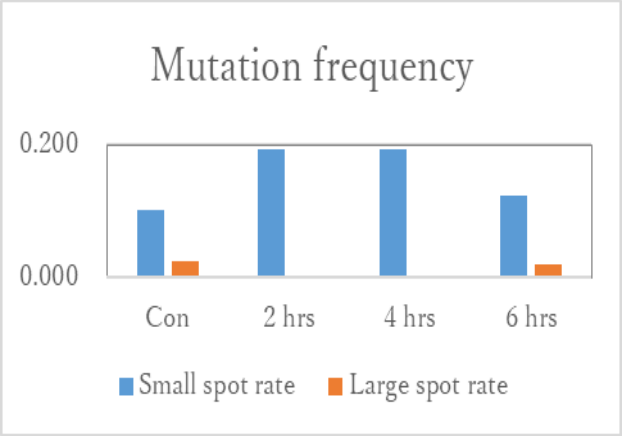

Fig. 1. Change of spot frequency by CTR (Teraherts wavelength). Spot frequency was calculated by small of large spot No./wing No.

REFERENCES:

[1] T. Takahashi *et al.*, Rev. Sci. Instrum., **69** (1998) 3770.

[2] S. Okuda and T. Takahashi, Infrared Phys. Technol., **51** (2008) 410.

[3] S. Okuda and T. Takahashi, J. Jpn. Soc. Infrared Science & Technology 25 (2016) 49 (in Japanese).

[4] S. Okuda Y.Tanaka and T. Takahashi, KUR Progress Report 2018, (2019) CO6-17.

[5] Y.Tanaka *et al.,* Eastern Medicine, 28 (2012) 21-35.

CO6-14 Structural analysis of multi-domain protein as studied by complementary use of molecular dynamics simlulation and small-angle X-ray scattering

R. Inoue, A. Okuda, M. Shimizu, K. Morishima, N. Sato, R. Urade, and M. Sugiyama

Institute for Integrated Radiation and Nuclear Science, Kyoto University.

INTRODUCTION:

Under physiological condition, it is well recognized that most of proteins including multi-domain proteins are not fixed to certain configurations but rather dynamically fluctuating due to their internal dynamics [1]. The internal dynamics of protein are considered to be deeply related to the development of their functions, hence characterization of internal dynamics such as time constant and spatial scales are essential for revealing the mechanism of their intrinsic functions. The advantage of small-angle X-ray scattering (SAXS) measurement is that it can study the structure of protein under near physiological condition: solution state, hence the possible dynamics in it is essentially observable from this technique. Recently, molecular dynamics simulation (MD simulation) enables to identify the internal dynamics of protein. Therefore, the complementary use of SAXS and MD simulation would offer the better opportunity for identifying the possible internal dynamics of protein. As a first step of work, we firstly performed structural analysis of four-domain protein through the complementary use of SAXS and MD simulation.

EXPERIMENTS:

The preparation and purification of four-domain protein should be referred to our future paper [2]. SAXS measurement was performed with NANOPIX (Rigaku Corporation, Japan). X-rays from a high-brilliance point-focused X-ray generator (MicroMAX-007HF, Rigaku, Tokyo, Japan) were focused with a confocal mirror (OptiSAXS) and collimated with a confocal multilayer mirror and two pinholes collimation system with the lower parasitic scattering, "ClearPinhole". The scattered X-rays were detected with a two-dimensional semiconductor detector (HyPix-6000, Rigaku, Tokyo, Japan). The sample-to-detector distance and wavelength of X-ray used for present work was 1320 mm and 1.542 Å, respectively. For removal of unfavorable aggregates from the sample solution, the laboratory-based SEC-SAXS System (LA-SSS) was employed to measure the SAXS profile in the Q range (0.01 $Å^{-1}$–0.2$Å^{-1}$) [3]. As for MD simulation, we performed both all-atom and coarse-grained MD simulation. All the measurement and calculations were performed at 25 ºC.

RESULTS: Figure 1 shows the SAXS of four-domain protein. Firstly, we compared the SAXS profile calculated from the snapshot of All-atom MD simulation to experimentally observed SAXS profile. The calculated SAXS profile could not reproduce the SAXS profile

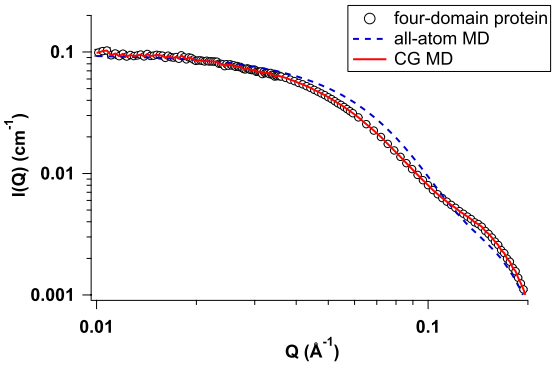

Fig. 1. SAXS profile of four-domain protein (circle). The dotted and continuous lines correspond to the calculated SAXS profile from the snapshot from all-atom MD and CG MD simulation, respectively.

adequately. We also calculated the SAXS profiles form several snapshots from all-atom MD simulation, however all the extracted snapshots could not reproduce the SAXS profile especially at the Q region lower than 0.10 $Å^{-1}$. It is expected that present all-atom MD simulation could not sample the possible configurations of four-domain protein within MD simulation time. Performing the longer time all-atom MD simulation is one of the solutions for improving the sample efficiency, however it will also increase the computational cost as well. In order to overcome such situation, we also performed coarse-grained MD (CG-MD) simulation. The advantage of CG-MD simulation is the increase of sampling efficiency due to coarse-graining an amino acid residue as a sphere. A snapshot was extracted from the trajectory of CG-MD simulation and the corresponding SAXS was calculated based on it. The calculated SAXS profile from CG-MD simulation is also included in Fig. 1. Compared to the result of calculation with all-atom MD simulation, the CG-MD derived SAXS profile could reproduce the SAXS results nicely, implying the high sampling efficiency with CG-MD calculation.

At present, we are trying to analyze the trajectory from CG-MD calculation to figure out the internal dynamics of this four-domain protein. It is expected that the complementary use of MD simulation and SAXS measurements will contribute to identify the functionally relevant internal dynamics of multi-domain protein.

REFERENCES:

[1] J. A. McCammon, and S. C. Harvey , Dynamics of Proteins and Nucleic Acids., (Cambridge University Press, 1987).

[2] A. Okuda *et al*., *in preparation.*

[3] R. Inoue *et al*., *Sci. Rep.,* **9** 12610 (2019).

CO6-15

Oligomeric structure and its temperature-dependent change of HspB1 from Chinese hamster ovary cell

M. Yohda, M. Nakamura, K. Morishima[1], R. Inoue[1], M.Sugiyama[1]

Department of Biotechnology and Life Science, Tokyo University of Agriculture and Technology
[1]Institute for Integrated Radiation and Nuclear Science, Kyoto University

INTRODUCTION: Small heat shock protein (sHsp) is a ubiquitous molecular chaperone with a relatively small molecular weight. The characteristic feature of sHsp is the α-crystallin domain, which is named after the α-crystallin in vertebrate lenses. Among mammalian sHsps, HspB1, also known as Hsp27, is the most ubiquitous one. Previously, we reported the structure and function of HspB1 from Chinese hamster (*Cricetulus griseus*) ovary cells (CgHspB1). SEC-MALS and SAXS analyses suggested the 16mer structure of CgHspB1 [1]. However, there exist several contradicting reports on the oligomeric structures of HspB1[2, 3]. HspB1 may take various oligomeric conformations. In this study, we analyzed the oligomeric structure of CgHspB1 by analytical ultracentrifuge (AUC). In addition, we examined the effect of the deletion of the C-terminal region and the N-terminal region.

EXPERIMENTS: CgHspB1 variants (WT, Wild type; S15D, phosphorylation mimic mutant; DelN, N-terminal deletion mutant; DelC, C-terminal deletion mutant) were expressed in *E. coli* and purified by anion exchange chromatography and size-exclusion chromatography. To suppress nonspecific hydrophobic interaction, size exclusion chromatography was carried out using a buffer containing 20% ethylene glycol. The oligomeric conformation of CgHspB1 variants were investigated by size exclusion chromatography on HPLC (SEC), electron microscopy, and analytical ultracentrifugation (AUC).

RESULTS: We speculated that the previous observations of various oligomeric conformations should be due to the nonspecific interaction by the hydrophobic surface of sHsp. Thus, we purified CgHspB1 variants by gel filtration chromatography using the buffer containing 20% ethylene glycol (Fig. 1). The purified WT and S15D exist as large oligomers and dissociate to small oligomers at the elevated temperature in SEC. DelN appeared as small oligomers without any temperature-dependent change. Curiously, DelN was digested into two fragments by protease. DelC appeared as various conformations. Then, WT and S15D were examined by AUC using a buffer containing 20% ethylene glycol. At 4°C, WT appeared as a single peak of 18mer (Fig. 2). The sedimentation coefficient increased as the elevation of temperature. At 40°C, it seemed to form 30mer. The conformation change is reversible. It changed to the original conformation by lowering the temperature. In addition, small oligomers of about 6mer and 12mer were also observed. Almost the same results were observed in S15D.

Based on these observations, we propose the following conformational change model. The structural unit of CgHspB1 is 6mer. In the inactivated condition, it assembles to 18mer. At the elevated temperature, they dissociate and reassemble to the activated conformations of 24mer or 30mer. They return to 18mer by lowering the temperatures. The N-terminal region is responsible for the assembly of 6 mers, and the role of the C-terminal region is the stabilization of oligomeric structures.

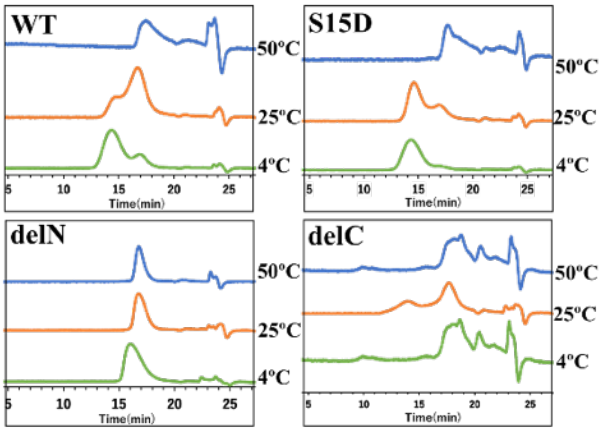

Fig.1 SEC analyses of CgHspB1 variants

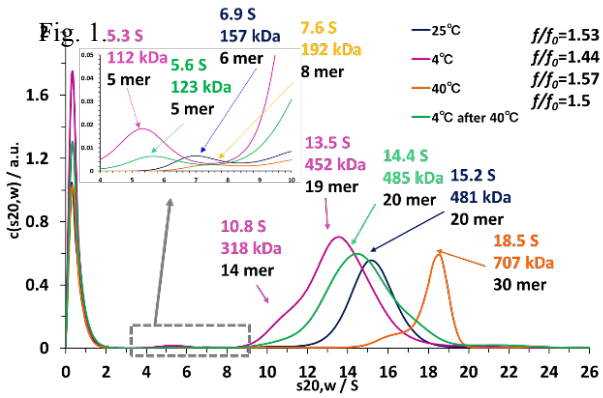

Fig. 2 AUC analyses of CgHspB1 WT

REFERENCES:

[1] E. Sha *et al.*, FEBS Open Bio., **9** (2019) 1826-1834.
[2] J. Behlke *et al.*, FEBS Lett., **288** (1991) 119-122.
[3] B. Lelj-Garolla *et al.*, J. Mol. Biol., **345** (2005) 631-642.

CO6-16 Quantitative analysis of contribution of tumor vascular damage to antitumor effect of X-ray using BNCR

K. Ono[1], T. Aihara[1], H. Tanaka[2], Y. Tamari[2], T. Watanabe[2], S. Suzuki[2], S. Masunaga[2]

[1]*Kansai BNCT Medical Center, Osaka Medical College*
[2]*Institute for Integrated Radiation and Nuclear Science,, Kyoto University*

INTRODUCTION: Tumor tissue consists of tumor cells and stroma, especially the vasculature that supplies the cells with oxygen and nutrients. The antitumor effect in BNCT is almost specific to cells accumulating boron compounds. In this study, we compare the effect of this tumor cell-specific BNCT with the effect of X-rays that has no tumor cell specificity, and quantitatively elucidate the effect of damage caused in the vascular system on the overall antitumor effect. This is the purpose of this research.

In fiscal 2019, prior to research on tumors, we conducted an experiment to confirm the effect of BNCR on normal tissue cells. This article reports the experimental results.

EXPERIMENTS: ***Mice and Irradiation of X-rays or neutron.*** 8-week-old C3H/He mice were prepared. The abdomen was irradiated with 10 Gy of photons 12 hours prior to the BPA-neutron irradiation. The rest of the abdomen was shielded with a lead plate. Two and half hours before neutron irradiation, ^{10}B-BPA in the form of a fructose complex (300 mg/kg body weight in terms of BPA) was subcutaneously administered to the mouse. The blood boron concentration at the time of irradiation was 15.2 ppm. The irradiation dose to the mouse was changed by changing the distance from the neutron beam exit hole in four steps, so that a single irradiation (30 minutes) gave four different doses. The control group of neutron irradiation alone was similarly irradiated. The highest neutron flux was 1.88×10^9/cm^{2}s. The flux was determined by the amount of activity induced in the gold foil.

Evaluation of radiation responsiveness using regeneration of intestinal crypt cells. Three and half days after neutron irradiation, a 10 cm long intestine was excised from the same predetermined site in the jejunum, and 3 specimens were cut out. After fixing with 10% formalin, histopathology microslide with HE staining was prepared, and the number of crypts in which regeneration was observed on the inner circumference of the intestinal wall was counted under a microscope.

Radiation sensitivity analysis. The relationship between the number of crypts in which regeneration was recognized and the neutron fluence was plotted in a semilogarithmic plot, and the slopes of the curves of the neutron alone group and the BPA-neutron group were compared. Since the doses of neutrons themselves and the amount of gamma rays accompanying them are equal at the same irradiation position, the difference in the slope is derived from the neutron reaction with BPA boron. The neutron fluence ϕ_0 similar to the dose D_0 was obtained, and the difference in ϕ_0 was converted into the dose due to the reaction of BPA boron and neutrons, and the D_0 at the boron-neutron reaction dose of BPA was obtained. Here, it was assumed that the concentration of boron in the crypt cells was equal to the concentration of boron in blood.

RESULTS and DISCUSSION: The results are shown in the figure. As can be seen in the figure, the ϕ_0 of the BPA-neutron irradiation group (closed circle), that is, the neutron fluence required to reduce the number of crypts by e^{-1}, is 0.925×10^{12}/cm^2. The D_0 calculated from this fluence value and the boron concentration of 15.2 ppm was 1.04 Gy. Data on such intestinal crypt susceptibility have not been reported yet, but are unexpectedly large. Incidentally, the D_0 of gamma rays is about 1.3 Gy. It is very interesting to see how the values obtained this time agree with the estimated value by N/C ratio of the cell (Ono's equation). However, this requires to know boron concentration in the crypt cell, and it is a future research topic. I believe that the high-precision α-autoradiography developed by Ono and Tanaka will be useful for that purpose.

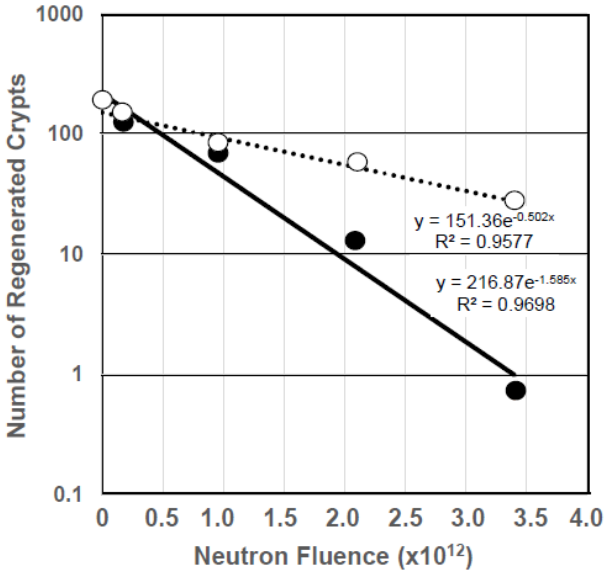

Closed circle: BPA+Neutron, Open circle: Neutron alone

REFERENCES:

[1] Eric J. Hall & Amato J. Giaccia, in Radiobiology for the Radiologist, 7th ed., 2012 by LIPPINCOTT WILLIAMS & WILKINS, a WOLTERS KLUWER.
[2] K. Ono, *et al.*, Journal of Radiation Research, Vol. 60, No. 1, 2019, pp. 29–36.
[3] K. Ono, *et al.*, Applied Radiation and Isotope Vol. 161, 2020, 109159.

CO6-17 Observation of Water Uptake in Alternate Grafting of Tomato and Eggplant using D_2O as Tracer

U. Matsushima, N. Kubota, D. Ito[1], Y. Saito[1] and H. Shono[1]

Faculty of Agriculture, Iwate University

[1]*Institute for Integrated Radiation and Nuclear Science, Kyoto University*

INTRODUCTION: Graft-incompatibility is known to increase hydraulic resistance at the grafted joint. Large hydraulic resistance at the grafted joint due to graft-incompatibility is expected to produce sweet tomato fruits by limiting water uptake. However, Such graft-incompatibility may cause plant death [1]. It is important to know how much water uptake can be limited by graft-incompatibility. We observed water uptake in alternate grafting of tomato and eggplant by using neutron imaging and deuterium oxide (D_2O) as tracer.

MATERIALS and METHODS: 4 kinds of grafted samples, including tomato grafted onto eggplant rootstock (T/E) and tomato rootstock (T/T), and eggplant grafted onto tomato rootstock (E/T) and eggplant rootstock (E/E) were prepared. Tomato (TO) and eggplant (EO) without grafts were prepared as control plants. The tomato and eggplant seedlings were grafted on the 23th of August 2019, after 29 and 30 days from sowing, respectively. Control samples were selected from the seedlings that were sown at the same time with seedlings for grafted plants. Four days after grafting, the samples were transplanted into glass tubes filled with glass beads in order to deliver quick D_2O supply. We performed neutron imaging at the E2 hole of Kyoto University Reactor (KUR) from the 3rd to the 5th of September. After removing water from the glass tube using a syringe, D_2O was injected into the glass tube. Immediately after the injection, interval neutron imaging was started. The exposure and interval times were 300 s and 360 s, respectively.

RESULTS: The neutron cross section of D_2O is much lower than that of water. On another note, chemical characteristics of D_2O is similar to water. Therefore, plant can uptake D_2O through the root system. In the presence of D_2O, neutron attenuation first decreased from the shoot part near the roots then toward the upper shoot part. The plant neutron image became brighter by increasing the D_2O content in it. Therefore, increasing the D_2O content in plant shoots can cause changes in neutron attenuation, which can be calculating by neutron imaging. The amount of change in the neutron attenuation coefficient is calculated as the difference in initial attenuation coefficient (μ) and that of at a certain time point (μ'). Changes in the neutron transmission coefficient is calculated using following equation:

$$\mu - \mu' = \frac{1}{x} \ln \frac{I'}{I}$$

The distance of neutron transmission x is equal to plant shoot diameter in this case. The initial neutron intensity I and that of at the certain time point I' are pixel value of those of the neutron images, respectively.

As a region of interest (ROI), we observed changes in the neutron attenuation coefficient with a plant shoot length of 5 mm near the roots. However, Plant transpiration indicated by D_2O uptake is highly influenced by plant size. Therefore, the changes in the neutron attenuation coefficient were compared by per dry mass (M_{dry}) of the samples. Figure 1 shows the history of the amount of the change in the neutron attenuation coefficient, $(\mu - \mu')/M_{dry}$. Significance

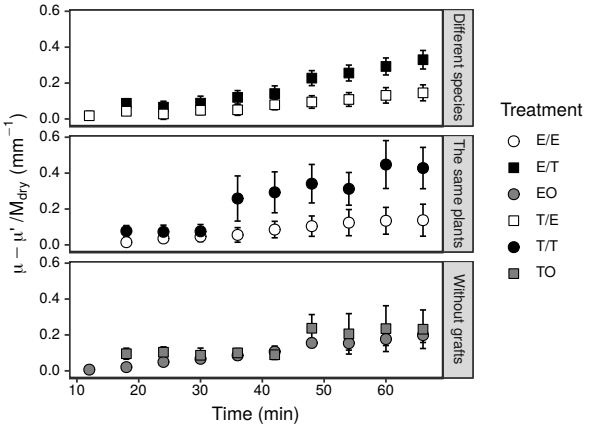

Fig. 1. History of the amount of change in the neutron attenuation coefficient, $(\mu - \mu')/M_{dry}$. Rows in matrix of the graphs were divided by 3 groups, namely grafted with different spices, grafted with the same plants, and without grafts.

tests were performed using the Tukey HSD test ($n = 3$). There was no significant difference between the six groups. The tomato and eggplant without grafts showed the same changes in neutron attenuation. The uptake of D_2O might be similar among tomato and eggplant when without grafts. On another note, samples that were grafted with the same plants variedly changed. It means that the wounds produced by grafting strongly influenced sample growth for those that were grafted with the same plants (T/T and E/E). Interestingly, the eggplant grafted on the tomato rootstock (E/T) showed the second highest change in neutron attenuation. In previous studies, eggplant grafted on tomato rootstock produced larger roots [1]. The large tomato roots of the E/T sample supposedly contributed to the increased D_2O uptake.

REFERENCES:

[1] M. Oda *et al.*, J. Japan. Soc. Hort. Sci., **74**(6), 458-463 (2005).

CO6-18 Production of medical radioisotopes using electron linear accelerator

S. Sekimoto, T. Ohtsuki

Institute for Integrated Radiation and Nuclear Science, Kyoto University

INTRODUCTION: A shortage in the supply of ^{99}Mo resulting from the shutdown of reactors used for its production is a global problem. Because ^{99}Mo is an indispensable source of ^{99m}Tc, which is used in nuclear medicine to make diagnoses using techniques such as scintigraphy and single photon emission computed tomography (SPECT), a stable supply of ^{99}Mo is vital. Therefore, production of ^{99}Mo by using neutrons or protons generated in accelerators has been investigated [1–3]. To separate ^{99m}Tc from ^{99}Mo produced by an accelerator, methods based on sublimation, solvent extraction, and ion-exchange column chromatography have been examined and developed [2,4–6]. In addition, Gopalakrishna et al. have reported the preparation of ^{99}Mo by the ^{100}Mo(γ,n) reaction using bremsstrahlung photons [6], followed by conventional solvent extraction using methyl ethyl ketone (MEK) and zirconium (Zr) molybdate gel to separate ^{99m}Tc. According to the regulations of the Japanese pharmacopeia, the extraction using organic materials and the gel method using heavy metal elements such as Zr are not approved for the ^{99m}Tc-separation methods. Additionally, it is also difficult and impractical to use the sublimation method, which requires complicated and/or large scale devices for the mass-production of pure ^{99m}Tc. Recently, Kaken Inc. developed a new method, known as the "technetium master milker" (TcMM). This technique can produce highly pure ^{99m}Tc at a maximum activity of 1.85×10^{13} Bq (500 Ci) per batch from ^{99}Mo of low specific activity [7]. We carried out the production of ^{99}Mo by the ^{100}Mo(γ,n) reaction using bremsstrahlung photons generated in an electron linear accelerator (LINAC), a technique that has not been investigated significantly in Japan. The amounts of ^{99}Mo produced at several electron energies (E_e) were examined. To separate ^{99m}Tc from the irradiated target, in this work, the TcMM was applied to the ^{99}Mo produced by LINAC, and the subsequent yield of ^{99m}Tc was evaluated.

EXPERIMETS: The TcMM applied to the irradiated natMoO3 pellets was essentially the same as that reported by Tatenuma et al. [7]

RESULTS: The results of the TcMM applied to the $^{nat}MoO_3$ pellets irradiated with bremsstrahlung photons are shown in Table 1. The activities of ^{99}Mo and ^{99m}Tc in the $^{nat}MoO_3$ solution prepared in the first step of the TcMM and the solution obtained from the final step of TcMM, and the chemical yield of ^{99m}Tc are presented in Table 1. The table header 'Run No.' 10-1 and 15-1 indicate the results for the solutions containing dissolved $^{nat}MoO_3$ pellets irradiated with bremsstrahlung photons of E_e's of 25 and 30 MeV, respectively. In contrast, 'Run No.' 10-2 and 15-2 are the results for the solution where transient equilibrium has been reached between ^{99}Mo and ^{99m}Tc after the initial milking of ^{99m}Tc in the 10-1 and 15-1 solutions. The chemical yield of ^{99m}Tc ranged between 83 to 99% over the four runs of the TcMM. In particular, the activity of ^{99}Mo in the solution collected by the TcMM was low, being below the detection limit of γ -ray spectrometry. This can also be confirmed by examining the γ-ray spectra of the $^{nat}MoO_3$ solution before the TcMM and the solution collected by the TcMM. Those spectra were reported in ref. [8].

REFERENCES:

[1] Y. Nagai *et al.*, J. Phys. Soc. Jpn., **82** (2013) 064201.
[2] Y. Nagai *et al.*, J. Phys. Soc. Jpn., **83** (2014) 08320.
[3] K. Nakai *et al.*, Proc. Jpn. Acad. Ser. **B 90** (2014) 413–421.
[4] M. Kawabata *et al.*, J. Phys. Soc. Jpn., **84** (2015) 023201.
[5] K. Mang'era *et al.*, J. Radioanal. Nucl. Chem., **305** (2015) 79-85.
[6] A. Gopalakrishna *et al.*, J. Radioanal. Nucl. Chem., **308** (2016) 431-438.
[7] K. Tatenuma *et al.*, Radioisotopes **63** (2014) 501-513.
[8] S. Sekimoto *et al.*, J. Radioanal. Nucl. Chem., **311** (2017) 1361-1366.

Table 1. Yield of ^{99m}Tc from bremsstrahlung photon-irradiated $^{nat}MoO_3$ by TcMM process.
([a] Second crop, [b] End of bombardment, [c] Detection limit)

Run No.	Weight of $^{nat}MoO_3$ & E_e	Elapsed time from EOB[b]	Activity in $^{nat}MoO_3$ solution (Bq)		Activity in solution collected by TcMM process (Bq)		Yield of ^{99m}Tc
		(h)	^{99}Mo	^{99m}Tc	^{99}Mo	^{99m}Tc	(%)
10-1	0.97 g, 25 MeV	213.2	4.91E+04	5.40E+04	<DL[c]	5.05E+04	93.5
10-2[a]		237.3	3.74E+04	3.98E+04	<DL[c]	3.33E+04	83.7
15-1	0.96 g, 30 MeV	215.3	1.15E+05	1.26E+05	<DL[c]	1.19E+05	94.2
15-2[a]		239.2	5.20E+04	8.48E+04	<DL[c]	8.33E+04	98.3

CO6-19 *N*-Acetylneuraminic acid functioned as the scavenger for reacive oxygen species generated by the gamma-ray irradiation

N. Fujii[1], S. Kishimoto[1] and T. Takata[2]

[1] *Radioisotope Research Center, Teikyo University*
[2] *Institute for Integrated Radiation and Nuclear Science, Kyoto University*

INTRODUCTION:

N-Acetylneuraminic acid (Neu5Ac) is a sialic acid, which occurs in mammals, certain mollusks, and some microorganisms, and is found a capping suger in the oligosaccharide chains of glycoproteins and glycolipids [1]. Most studies on glycanic Neu5Ac have focused primarily on cell protection, fertilization, immunology, inflammation and tumors [2-4]. Free Neu5Ac molecules is oxidized by H_2O_2 to provide its decaroxy product, 4-(acetylamino)-2,4-dideoxy-D-glycero-D-galacto-octonic acid (ADOA) [5]. Therefore, monomeric Neu5Ac is the potent defense molecule against oxidative damage.

Ionizing radiation decomposes water and generates free radicals and reactive oxygen species. Then we expected the monomeric Neu5Ac might be scavenged the reactive oxygen species generated the ionizing radiation. In this study, we developed the method to quantitate the potential scavenging reaction of Neu5Ac for gamma-ray irradiation. In order to test our methods, we irradiated Neu5Ac solution with gamma-ray, then quantitated product (ADOA) by liquid chromatography–tandem mass spectrometry (LC-MS/MS) using by our developed method.

EXPERIMENTS:

Material Nu5Ac was dissolved in water, and the pH of the solution was adjusted to 7.0 with sodium hydroxide.

Gamma-irradiation Gamma-irradiation was carried out at the Co-60 Gamma-ray Irradiation Facility of the Kyoto University Institute for Integrated Radiation and Nuclear Science. Nu5Ac aqueous solution were irradiated with gamma ray at a dose rate of 943 Gy/h.

Quantitation of ADOA The quantitative analysis of ADOA was used by LC-MS/MS. The high performance liquid chromatography was used a U3000HPLC system (Thermo Fisher scientific). The column was CAPCELL CORE PC (OSAKA SODA, 2.7 μm, 2.1 mm I.D.×100 mm). A sample were eluted with a flow rate of 0.2 mL/min and an isocratic mode with mobile phase (75% acetonitrile, 25% water, 10 mM ammonium formate, pH 3.5). The mass spectrometer was used Q Exactive (Thermo Fisher scientific). ADOA was measured by parallel reaction monitoring (PRM) in the positive ion mode, using transitions m/z 282.11 → m/z 186.07

RESULTS:

To quantitatively investigate the amount of ADOA, PRM method was set the optimal for commercial standard. Then, the method was used for Neu5Ac aqueous solution after gamma-ray irradiation.

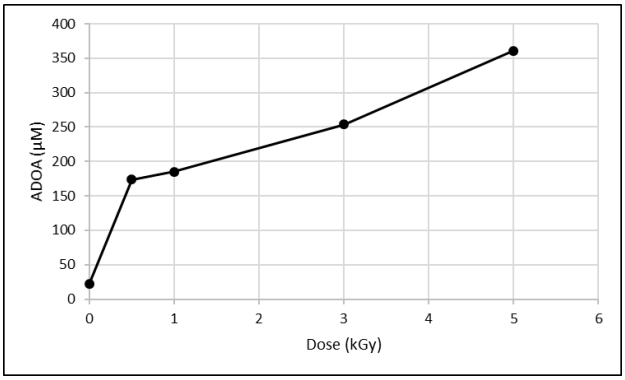

Fig. 1. Production of ADOA from Neu5Ac by irradiation with gamma-ray

Fig. 1 show the production of ADOA from 100mM Neu5Ac aqueous solution irradiated with gamma-ray at doses of 0, 0.5, 1, 3 and 5 kGy. As the radiation dose was increased, the production of ADOA increased. The 1 kGy gamma-ray irradiation for 100 mM Neu5Ac solution increased the ADOA amount to 184 μM (Fig. 1), suggested the yields of ADOA from Nu5Ac was 0.184 %. On the other hand, in 10 mM Neu5Ac solution, the yields of ADOA from 1kGy gamma-ray irradiation was 1.34 % (data not shown). The lower concentration of substrate, the higher yields of ADOA, suggested that gamma-ray promotes reaction from Neu5Ac to ADOA via formation of reactive oxygen species (H_2O_2) in solvent (indirect action).

Those results suggested monomeric Neu5Ac as scavenger for reactive oxygen species generated by the gamma-ray irradiation.

REFERENCES:

[1] R. Schauer R., *Zoology*, **107** (2004) 49-64
[2] T. Angata *et al.*, *Chem. Rev.* **102** (2002) 439-469
[3] R. P. Crocker, *Curr. Opin. Struct. Biol.* **12** (2002) 609-615
[4] K. Takayama *et al.*, *Proc. Natl. Acad. Sci. USA* **93** (1996) 10662-10667
[5] R. Iijima *et al.*, *FEBS Lett.* **561** (2004) 163-166

CO6-20 Preliminary analysis of structural composition of menaquinone-7 produced by *Bacillus subtilis natto*

T. Chatake, Y. Yanagiswa[1], A. Okuda, K. Morishima, R. Inoue, M. Sugiyama

Institute for Integrated Radiation and Nuclear Science, Kyoto University
[1]Faculty of Pharmaceutical Science, Chiba Institute of Science

INTRODUCTION: Natto is a Japanese traditional fermented food, which is made of soybeans. It attracts a great attention from the point of view of nutrition, because it contains various kinds of physiologically active substances. In particular, menaquinone-7, which is a kind of vitamin K_2, is abundantly contained in natto [1]. In Japan, young women intake 99% of menaquinone-7 from pulses including *natto*, and the pulse food is the main source of vitamin K (45.1%) for the *natto* eater of the young Japanese women [2]. Menaquinone-7 produced by *Bacillus subtilis natto* (*natto*-MK-7) has a remarkable physiochemical property. All types of vitamin K are water-insoluble compounds. Meanwhile, *natto*-MK-7 is a water-soluble macromolecular complex, of which molecular weight is estimated to be 80~100 kDa by size-exclusion chromatography [3,4]. This property has an advantage on application of food/medical uses: pharmaceutical preparation, supplements, and food manufacture. Previously, Ikeda and Doi reported that the complex is composed of ~3kDa glycopeptides named K-binding factor (KBF) [3]. Our recent study of highly purified *natto*-MK-7 indicated an additional component with the molecular weight of ~11 kDa [5]. However, the detail information about the structural components of natto-MK7 is still unknown. In the present study, mass spectroscopy of *natto*-MK7 has been succeeded. Here, our new finding is shown.

EXPERIMENTS: *Natto*-MK-7 was produced and purified as previously reported [5]. *Bacillus subtilis natto miyagino* was incubated in liquid medium containing 2% hipolypepton-S, 3% glycerol, and 0.5% methionine. After cultivation at 42 °C with shaking at 100 rpm for 7 days, liquid medium was concentrated before purification. The purification was carried out by fast protein liquid chromatography. Four times of weak anion-exchange chromatography using DEAE sepharose FF were carried out with a gradient from 0.3 M to 1.0 M NaCl in 20 mM Tris-HCl buffer (pH 7.6). The final step of the purification was size-exclusion chromatography using GE HiPrep 16/60 Sephacryl S-300HR in 20 mM Tris-HCl buffer (pH 7.6) and 0.1 M NaCl. Mass spectroscopy was measured by MALDI-TOF/MS (microflexLT).

RESULTS: As shown in Fig. 1, mass spectra of *natto*-MK-7 could be observed for the first time. Strong peaks with m/z < 600 are derived from the matrix used for TOF/MS. Significant peaks could not be observed at m/z > 10,000, indicating that the whole structure of *natto*-MK-7, of which molecular weight was presumed to be 80~100 kDa, was not observed. A peak with m/z = 656 corresponds to menaquinone-7 (MW~650). Most significant peaks were around m/z = 1050, implying that KBF is smaller than 3kDa, of which value was estimate by SDS-PAGE. In addition, the plural number of the peaks suggests the variation of the amino acid sequences of KBF.
It is just the first data of mass spectroscopy of *natto*-MK-7. The further experiments are under planning.

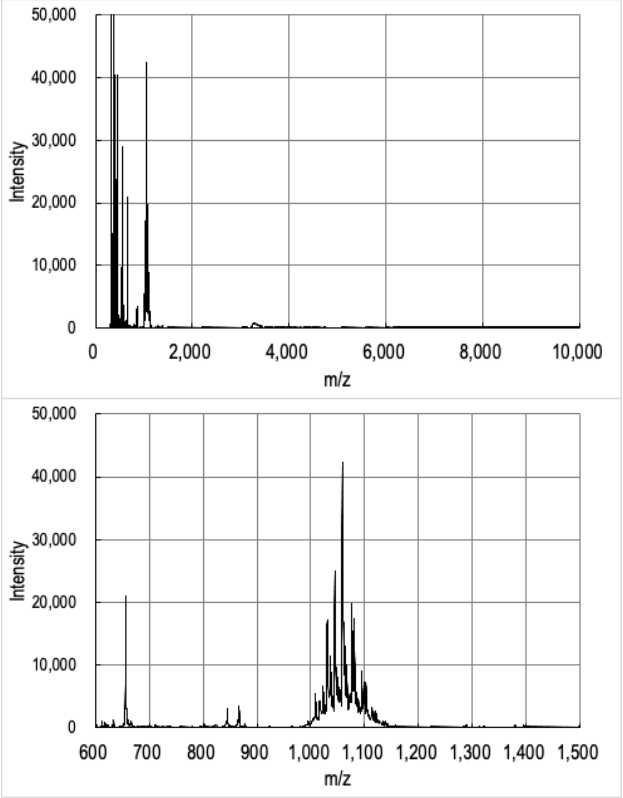

Fig. 1. The results of mass spectroscopy of natto-MK-7 in the ranges of 0~10,000 Da (upper) and 600~1,500 Da (lower).

REFERENCES:

[1] D.H. Bishop, K.P. Pandya, H.K. King, Biochem. J. **83**, 606-614 (1962).
[2] M. Kamao *et al.*, J. Nutr. Sci. Vitaminol (Tokyo) **53**, 464-470 (2007).
[3] H. Ikeda, Y. Doi, Eur. J. Biochem. **192**, 219-224 (1990).
[4] Y. Yanagisawa, H. Sumi, J. Food Biochem. **29**, 267-277 (2005).
[5] T. Chatake *et al.*, Y. Yanagisawa, R. Inoue, M. Sugiyama, T. Matsuo, S. Fujiwara, J. Food Biochem. e12630(6) 1-7 (2018).

CO6-21 Measurement of Absorption Spectra of a Humann Calcified Aorta Tissue in the Sub-Terahertz Region, which Dependented on the Thickness (III)

N. Miyoshi and T. Takahashi[1]

Department of Molecular Chemistry, Kyoto Institute of Technology
[1]Institute for Integrated Radiation and Nuclear Science, Kyoto University

INTRODUCTION: The LINAC (Electron linear accelerator) technology in the millimeter- and terahertz-waves had been unique and had been used as a coherent synchrotron light source in the Institute for Integrated Radiation and Nuclear Science of Kyoto university (KURNS) to observe the transmittance spectra of a human calcified aorta tissue as a collaborate study. The absorption spectra in the sub-terahertz region had been not so clear for the raw tumor tissue although Ashworth-PC. *et al.* [1] had reported for the excised human breast cancer by a terahertz pulsed spectroscopy observed at 320 GHz, which was estimated a longer relaxation time component of the induced electricity for water molecules [2-3] in the raw tumor tissue for three years at the linear analysis.

We had started to measure of new biological sample of a calcified human aorta dried tissue sampling from the pathological autopsy in the last year. Furthermore, the getting spectral information was estimated with the SEM-EDX elements images of the calcified aorta tissue with a biological meaning in this year. It was reported the relation of the biological information between both of the element images and sub-THz spectral components in this report.

EXPERIMENTS: (1) Instrument of Near-field in Terahertz Region: The photograph of the instrument was shown in Fig. 1. Mark-A: Pre-probe Wiston cone; 50-10mm diameter, Length=60mm; the irradiate diameter=0.775mm; Mark-B: The concentrate light probe (diameter=3mm). The instrument was developed by Dr. T. Takahashi [4] for the transmittance measurements.

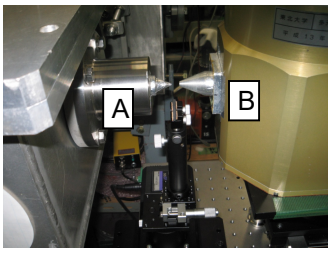

Fig. 1. The near field area of sample holder position.

(2) Measurement of the Thickness of Sample: .
The thickness on the three points was measured by a laser spot type (CL-P030, Keyence, Osaka, Japan).

RESULTS and DISCUTION: (1) The thickness of samples on the three points were measured as shown inf Fig. 2. A (calcified deposition) =0.0929, B (cholesterol deposition) =0.837, C (protein deposition) =0.379 mm, respectively.

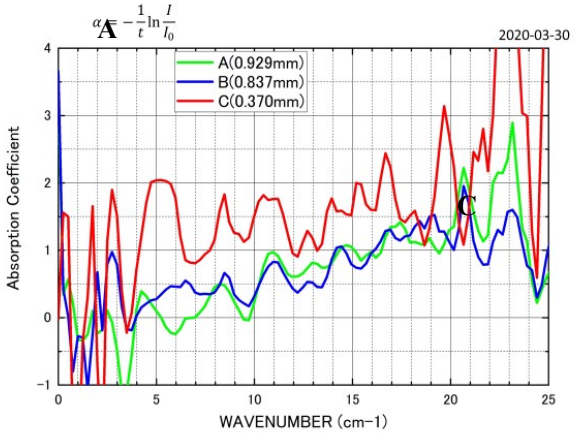

Fig. 2. The absorption spectra at 3 points (A: calcified point), the (B: cholesterol deposition, C: protein deposition) of a human aorta blood vessel wall, respectively.

(2) The absorption spectra of the sample tissue for each points A, B and C were measured according the different thickness points as shown in Fig. 2, which might be changing the refraction to dependent on the thickness values. It was different from the last reported spectra a little.

In the results, the absorbance of the dried tissue at 248 and 522 GHz were observed in the calcified area (included of $CaPO_4$ components from the data of SEM-EDX analysis of calcified aorta tissue), and the absorption peaks of 330, 620 GHz were observed in the cholesterol adhesion area. In the both areas, it was observed the absorption peaks at 500 and 659 GHz also.

In this report, it can report of more detail analysis combined with the thickness information data of the dried tissue by an laser measurement technology.

REFERENCES:

[1] Phillip C. Ashuworth *et al.*, Optics Express, **17** (2009) 12444-12454.
[2] Toshiko Fukasawa, *et al.*, Phys. Rev. Lett., **95** (2005) 197802.
[3] Hiroyuki Yada, *et al.*, Chem. Phys. Lett., **464** (2007) 166-170.
[4] T. Takahashi, *et al.*, J. Phys.: Conf. Ser. **359** (2012) 012016-1-4.